catalysts

MDPI

Article

Photocatalytic Evaluation of the Ternary Composite $CdSO_4$-ZnAl LDH/ZnS in Hydrogen Production without a Sacrificial Reagent

Angela G. Romero-Villegas [1], Clara Tzompantzi-Flores [1], Raúl Pérez Hernández [2], Arturo Barrera-Rodríguez [3], Francisco Tzompantzi [1,*] and Ricardo Gómez [1]

[1] Departamento de Ecocatálisis, Universidad Autónoma Metropolitana-Iztapalapa, México City 09340, Mexico
[2] Departamento de Estudios del Ambiente, Instituto Nacional de Investigaciones Nucleares, México City 52750, Mexico
[3] Centro de Investigación en Nanocatálisis Ambiental y Energías Limpias, Universidad de Guadalajara, Ocotlán 47820, Mexico
* Correspondence: fjtz@xanum.uam.mx

Abstract: In this work, a layered double hydroxide support modified with cadmium was synthesized by a one-pot coprecipitation method. Then, it was sulfured in different percentages by a solvothermal method. Next, the samples were analyzed using various characterization techniques like XRD, DRS, FTIR, N_2 physisorption, PL spectroscopy, TEM, and SEM. Finally, the synthesized and uncalcined materials were assessed in hydrogen production from water and a methanol-water solution under UV-light irradiation. The results showed that the sulphuration improves the photocatalytic activity, reaching a maximum rate constant of hydrogen production of 7403 μmol/g·h in a methanol-water solution and 1326 μmol/g·h in water.

Keywords: hydrogen production; photocatalysis; ZnS; LDH; sacrificial reagent

Citation: Romero-Villegas, A.G.; Tzompantzi-Flores, C.; Hernández, R.P.; Barrera-Rodríguez, A.; Tzompantzi, F.; Gómez, R. Photocatalytic Evaluation of the Ternary Composite $CdSO_4$-ZnAl LDH/ZnS in Hydrogen Production without a Sacrificial Reagent. *Catalysts* **2023**, *13*, 593. https://doi.org/10.3390/catal13030593

Academic Editors: Quyet Van Le, Dung Van Dao, Pankaj Raizada and Marcos Fernández García

Received: 15 February 2023
Revised: 7 March 2023
Accepted: 13 March 2023
Published: 16 March 2023

1. Introduction

Nowadays, a critical environmental issue affecting both developed and developing countries, meaning an elevated risk for living human beings, is air pollution originated by several manufactural emissions. Some of the air pollutants with a high presence in the atmosphere are lead, carbon monoxide, sulfur oxides, nitrogen oxides, and hydrocarbons. Their principal origin sources are sectors such as transport, energy waste management, construction, and agriculture. Moreover, these manufacturing and service sectors have in common the use of hydrocarbons as the principal energy generator, representing the world's first cause of air pollution. In this sense, it becomes a primary task to replace the use of fossil fuels and take action to reduce the concentration of pollutants in the air.

Hydrogen is the most abundant element; it can be found in 75% of the matter forming the universe, commonly obtained in gaseous form. Its use to produce energy is considered an ecologic alternative because it only emits water steam in a combustion reaction. Thus, the harmful emissions in the air are reduced. However, unfortunately, hydrogen is not the principal energy source; these are the hydrocarbons.

A benefit of using hydrogen is that this gas can be produced from renewable and non-renewable resources. Moreover, it has a high heating power of 120.011 kJ/kg, which is 2.7 times higher than the gasoline value (43.950 kJ/kg) [1].

Currently, one of the cheapest techniques for hydrogen production is photocatalysis. Although photocatalytic processes must have basic requirements to carry out, an advantage is that non-drastic conditions are necessary, which makes photocatalysis an attractive option to produce hydrogen. In the photocatalysis technique, a semiconductor material

must be irradiated with UV, visible, or NIR light to promote the formation of highly reactive species, such as free radicals, originating oxidation and reduction reactions [2].

Unlike other techniques employed for hydrogen production, such as chemical reforming, the photocatalytic processes reduce the emitted carbon dioxide amount. Thus, pollutant emissions are diminished in the hydrogen combustion process to generate energy and in hydrogen production. This critical reduction of the air pollutants in hydrogen production is due to the soft operational conditions not requiring elevated temperatures to carry out the process; in photocatalysis, it is possible to obtain hydrogen under environmental conditions, even under sunlight irradiation. An additional benefit is a relatively easy way to modify the photocatalysts' structure, texture, morphology, and composition, increasing the photocatalytic efficiency.

The basic requirements for a photocatalyst to produce hydrogen are that the valence band value must be higher than the water oxidation potential ($E_{O2/H2O}$, V vs. NHE) and the conduction band value lower than the hydrogen reduction potential ($E_{H2/H2O}$, V vs. NHE) [3]. Nevertheless, other factors must also be studied, such as the kind of material, the possible scavenger reagents employed in the reaction, the photocatalyst load, and the pH value in the reaction media, among others.

A current challenge in photocatalysis is to slow the charge carrier recombination (photogenerated species hole/electron) because a fast recombination results in deficient hydrogen production. To obtain a significant amount of hydrogen, various researchers have studied systems in which the following arrangements are favored: heterojunctions, Z scheme, oxides, and layered double hydroxides, among others.

Layered double hydroxides (LDHs), called clays or hydrotalcites, present at least two types of metallic cations. Layers constitute these kinds of materials, and they can present anionic species in the interlaminar hollow, or anionic species can interchange some species from the structure [4].

The general chemical composition of the LDHs is $[M^{2+}_{(1-x)}\ M^{3+}_{(x)}\ (OH)_2]^{x+}\ (A^{n-})x/n.\ mH_2O$, where M^{2+} and M^{3+} are divalent and trivalent ions with a positive charge; A^{n-} represents the ions with a negative charge, and they are placed in an intercalated arrangement between the brucite layers (positively charged); x is the charge density of the layer $[M^{3+}/(M^{2+} + M^{3+})]$, which is approximately 0.2–0.33; finally m is the number of water molecules in the interlaminar region plus the anions present in this area. Figure 1 shows a typical structural scheme for hydrotalcite materials.

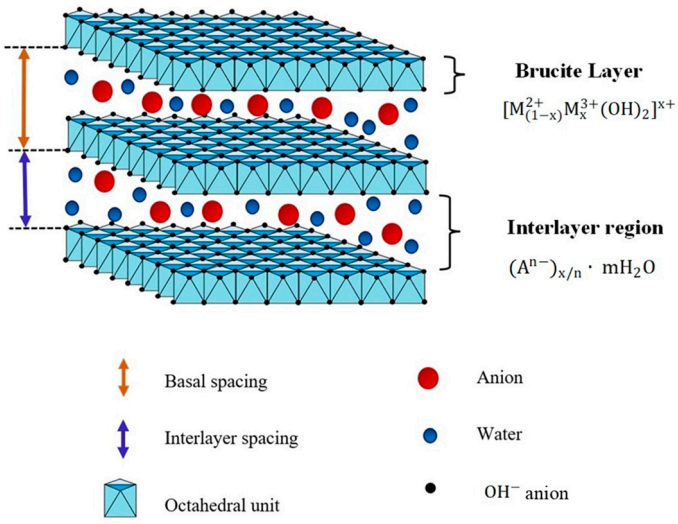

Figure 1. Structural scheme for hydrotalcite materials. Adapted from H Kaur et al. [5].

LDHs have been employed as heterogeneous photocatalysts in the absorption of pharmaceutical compounds, pollutants photodegradation [6], water splitting [7], and chromium reduction [8], among others.

LDH materials have been successfully synthesized using several techniques such as hydrothermal synthesis, sol-gel, electrosynthesis, anion interchange, and coprecipitation.

Numerous authors prefer this last synthesis method because it allows a straightforward modification of the structural parameters, the molar ratio M^{II}/M^{III}, and the metal cations and interlayer anion nature. Moreover, it permits the acquisition of substantial amounts of material at viable costs.

Some studied hydrotalcite materials are Zn-Al, Mg-Al, and Co-Al. However, these can be modified when Al is substituted by another cation, such as in the Zn-Al-Cr system. This has been used in the photochemical oxidation of NO [9]. Another strategy aimed at toluene remotion is focused on O substitution by Mn [10].

Noteworthy, there are many advantages to the LDHs use. For example, they are materials of low cost, they present null toxicity, the synthesis is fast and easy, and the modification by ionic interchange is feasible [11].

Cadmium is a metal with high toxicity for soil and water; it can affect the environment and human health. Nevertheless, cadmium (Cd) has several uses in the industry and is indispensable. In this sense, it is necessary to devise strategies to reduce cadmium concentration in the environment. An interesting alternative is to use the metal in photocatalysts for a second use; some studies have shown that CdS is efficient in pollutant photodegradation and water splitting. The E_g value, the conduction band, and the valence band positions lend the use of CdS for both processes. Furthermore, cadmium's high stability makes its elimination difficult in the environment, and it can be an advantage for photocatalysts because it would provide this quality to the material.

On the other hand, it has been shown that the sulfur addition in the hydrotalcite photocatalyst improves the photocatalytic activity in the hydrogen production, reaching a hydrogen production rate of 1599 μmol h^{-1} g^{-1} under UV light irradiation and using a methanol-water solution (50-50 vol%) [12].

In this work, layered double hydroxides ZnAlCd were synthesized by the chemical coprecipitation method. Next, these were modified through sulfur addition (S^{2-}) by the solvothermal method. Then, the materials were characterized by several techniques. Finally, the synthesized materials were assessed in hydrogen production under UV light irradiation from a methanol-water solution (50-50 vol%) without sacrificial reagent.

2. Results

2.1. X-Ray Diffraction

As shown in Figure 2, X-Ray Diffraction patterns show good crystallinity for the materials. The samples ZAC, ZAC-60S, and ZAC-80S exhibited diffraction peaks in the planes (003), (006), (012), (015), (018), (110), and (113), indicating the presence of ZnAl LDHs (COD ID: 9015034). Additionally, the samples showed at 12° of 2 Theta the plane (200) of hydrozincite (COD-ID: 9007481), which is labeled as HZT (▲). The presence of both materials is possible because the samples were synthesized at 98 °C and dried at 80 °C. Then, the generated amount of the LDH material depends on the limiting reactant $Al(NO_3)_3$, and the formation of hydrozincite occurs because $Zn(NO_3)_3$ is an excess reactant that reacts with urea in excess too.

The presence of sulfur in the samples ZAC-60S and ZAC-80S was confirmed by the broad diffraction signal exhibited at 29° of 2 Theta; this matches the plane (111) of zinc sulfide (COD ID: 1100043), which is labeled as ZnS (♦). For the sample ZAC-100S, a complete change in the material's structure was observed; the obtained diffractogram suggests that most of the Zn^{2+} cations reacted with sulfur to get ZnS in a high percentage. Nevertheless, the plane (003) remains visible with a weak signal at 11° of 2 Theta, confirming the presence of the ZnAl-LDH material in a minor percentage.

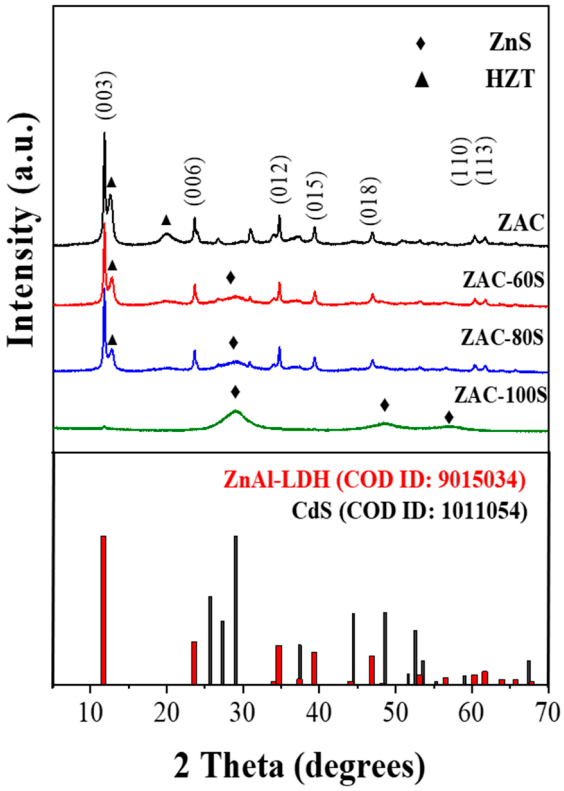

Figure 2. X-ray Diffraction patterns of the ZnAl LDH samples modified with cadmium and sulfur.

X-ray Diffraction did not confirm the cadmium presence, possibly because ZnS and CdS have similar reflection planes. Table 1 registers the lattice parameters for the synthesized samples. The interplanar spacing "d", the crystal size, and the parameters "a" and "c" were determined for ZnAl-LDH in the plane (003). The parameters were determined for a hexagonal lattice; they correspond well with the values published in previous papers, in which a molar ratio of Zn:Al 3:1 was used [13,14]. The average values for the lattice parameters were d = 7.53 ± 3 Å, a = 3.06 Å, and c = 22.60 ± 0.08 Å.

Table 1. Crystalline information for the samples, types ZnAl-LDH and ZAC-XS.

Material	Lattice Parameters (Å)			Crystal Size (nm)
	$d_{(003)}$	$a = 2 \times d_{(110)}$	$c = 3 \times d_{(003)}$	
ZAC	7.55	3.06	22.65	27.58
ZAC-60S	7.55	3.06	22.65	31.59
ZAC-80S	7.56	3.06	22.68	25.47
ZAC-100S	7.50	—	22.52	11.39
Material	$d_{(111)}$	$a = (4 \times r/2^{0.5})$	a = b = c	Crystal size (nm)
ZAC-100S	3.1	5.6	5.6	37.8

Additionally, the lattice parameters for the sample ZAC-100S were determined in the plane (111) for a face-centered cubic structure of ZnS, and an atomic radius (r) of 0.100 nm for ion sulfur was used. The cubic lattice exhibited an interplanar spacing d = 3.1 Å and a = 5.6 Å; the results agree with the literature [15]. This information is presented because diffractograms in Figure 2 show that ZnS has a major presence in the sample than ZnAl-LDH material.

The crystallographic parameters in Table 1 show that in the ZAC-60S and ZAC-80S, the lattice did not exhibit substantial changes when sulfur was added; the lattice kept its structure. Nevertheless, for the sample ZAC-100S, the ZnAl-LDH material in the plane

(111) showed a minor distance in the interlaminar spacing, d = 7.50 Å, the same as that of the parameter "c" with 22.52 Å. These indicate that some layers in ZnAl-LDH have collapsed by the loss of hydroxyl groups responsible for the laminar arrangement.

Regarding the crystal size, the largest crystallite size (31.59 nm) for the materials ZnAl-LDH was observed in the sample with the lowest amount of S^{2-} (ZAC-60S), and the smallest crystallite size (11.39 nm) was obtained in the sample with the highest amount of S^{2-} (ZAC-100S). This suggests that the sample ZAC-60S has the smallest superficial area for photocatalytic reaction, whereas the ZAC-100S has the largest.

2.2. Diffuse Reflectance Spectroscopy (DRS)

Figure 3 shows DRS spectra for the synthesized materials. As can be observed, the bare sample ZAC showed an absorption edge at 190 nm. On the other hand, for the sulfured samples ZAC-60S, ZAC-80S, and ZAC-100S, it was observed that a higher intensity of reflectance and the absorption edges shifted at higher wavelengths (~310 nm). This behavior suggests that the sulfured materials have a stronger light absorption.

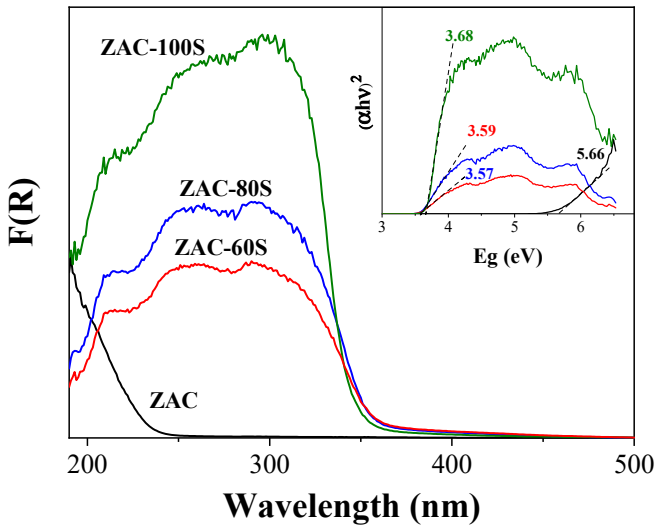

Figure 3. Diffuse reflectance spectra and band gap energy determination of the ZnAl-LHD type materials and ZAC-100S.

The band gap energy for the samples was determined by Tauc-plot from a modified Kulbelka–Munk equation (Equation (1)), where E_g is the band gap energy (eV), h is the Planck constant, B is the absorption constant, ν is the frequency of the electromagnetic radiation (s^{-1}), and α is the extinction coefficient that is proportional to F(R). Data for the Tauc-plot were determined considering an indirect allowed transition where n = 2.

$$\alpha(h\nu) \approx B(h - E_g)^n \quad (1)$$

The values of E_g were determined by plot $\alpha(h\nu)^2$ vs. hv and extrapolating linearly the absorption edge toward the abscissa's axis. Figure 3 shows that the bare sample ZAC exhibited the highest band gap energy at 5.66 eV; according to the literature, ZnAl-LDH material exhibits a band gap energy at 3.1–3.8 eV [7,12]. The wide band gap energy for ZAC is explained by hydrozincite presence; the band gap energy reported by hydrozincite is ~5 eV [16]. Sulfured samples ZAC-60S, ZAC-80S, and ZAC-100S exhibited the energy band gap values of 3.57, 3.59, and 3.68 eV, respectively; those agree with the values reported for ZnAl-LDH and ZnS [17]. A benefit to low band gap energy materials is that the electrons are promoted more easily to the conduction band, and thus the probability for electron-hole pair formation is higher.

2.3. Fourier Transform Infrared Spectroscopy (FTIR)

Figure 4 shows the IR spectra of the synthesized materials. The samples presented characteristic vibrations at 3399 cm^{-1} corresponding to the hydroxyl group [18].

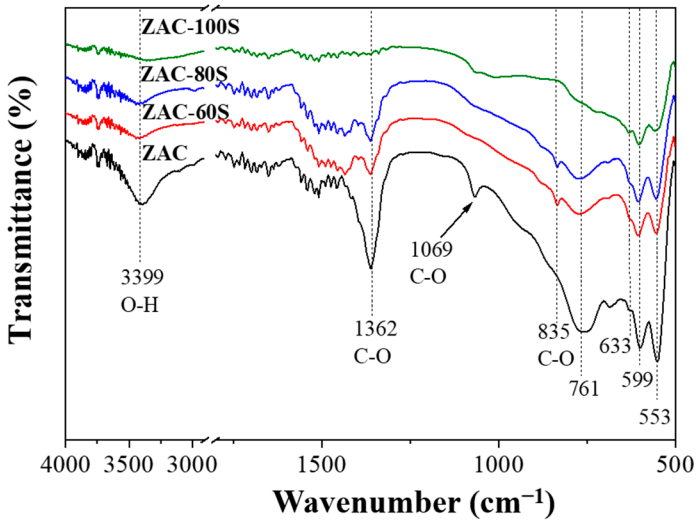

Figure 4. Fourier Transform Infrared Spectra for the samples ZnAl-LDH samples and ZAC-100S.

The sample ZAC-100S showed the weakest signal at 3999 cm^{-1}; this was attributed to a minor concentration of the hydroxyl group in that sample that lead to the slight lattice contraction observed in XRD (Table 1). Thus, it is confirmed that the specie is responsible for keeping the laminar arrangement.

The bands observed at 1362, 1069, and 835 cm^{-1} correspond to different vibrational modes of carbonate ions [3]. As can be seen, the sample ZAC shows a major presence of these species. The hydrozincite has the same laminar arrangement as the ZnAl-LDH materials with a slight difference; for hydrozincite, the carbonate ions are responsible for keeping the laminar arrangement. In this sense, for the sample ZAC, the XRD, FTIR, and DRS results show that hydrozincite is present in this sample. In contrast, the FTIR spectra for the samples ZAC-60S and ZAC-80S show carbonate ions with lower percentages of transmittance in their bands. For the sample ZAC-100S, the carbonate ions presence was not observed. This implies that hydrozincite formation is inhibited when S^{2-} is added.

The vibrations observed between 500–600 cm^{-1} are matched to metal-oxygen-metal bonds in the ZnAl-LDH, which confirms the presence of Zn-Al bonds [19]. On the other hand, the bands at 761 and 633 cm^{-1} correspond to the Al-OH and Zn-OH bonds, respectively [14]. For the sample ZAC-100S, the bands at 761 cm^{-1} are not visible because the ZnAl-LDH formation is not favored, as revealed by the XRD technique.

2.4. Photoluminescence

Figure 5 shows the photoluminescence spectra; they were recorded for an excitation wavelength of 299 nm. As can be seen, the sample ZAC exhibited the highest photoluminescence intensity, indicating the high electron/hole rate recombination. The absorption bands observed at 469 nm correspond to vacancy formation. The scale modification in the XY-axes showed that the sample ZAC-100S has the slowest rate of electron-hole recombination; this is attributed to a high percentage of vacancies in the material, which can improve photocatalytic performance [20].

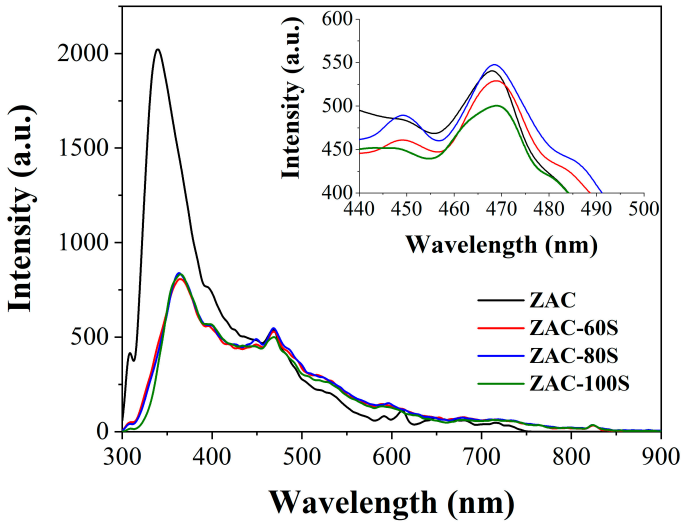

Figure 5. Photoluminescence spectra of the sulfured ZnAlCd materials.

2.5. N_2 Physisorption

The N_2 adsorption-desorption study exhibited isotherms type IV (Figure 6), which correspond to mesoporous materials with an H3 hysteresis loop associated with laminar materials; this agrees with a previous report for materials ZnAl-LDH [6]. Table 2 shows the synthesized materials' specific surface area (SBET). As can be seen, the sulfur addition to the samples makes the available specific surface area larger. Although XRD explains this, the crystal size of the ZnAl-LDH material is smaller in the samples ZAC-80S (25.47 nm) and ZAC-100S (11.37 nm) than in ZAC (27.58 nm). On the other hand, the sample ZAC-60S has a larger crystal size than ZAC; therefore, a minor specific surface area was expected, but it was larger. Thus, although for ZAC-60S, the area contributed by the ZnAl-LDH material will be smaller, the area contributed by the ZnS must be considered. This is the reason why the sample shows a large specific surface area.

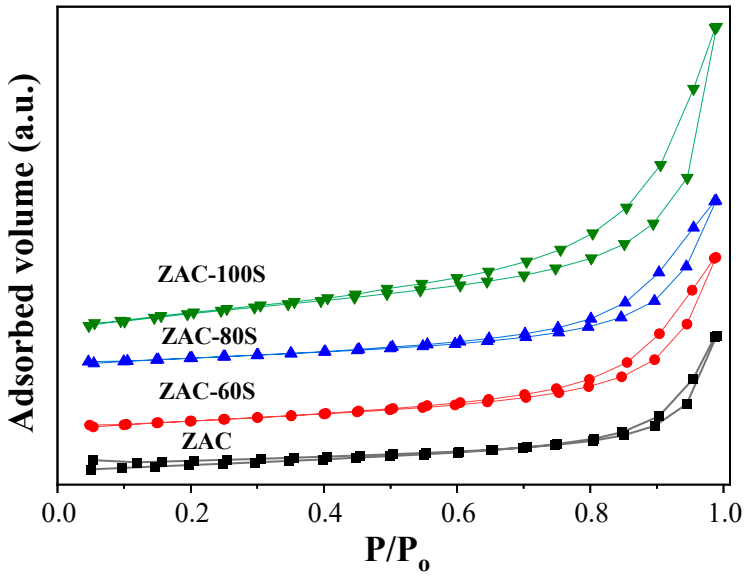

Figure 6. N_2 physisorption isotherms for the ZnAlCd sulfured samples.

Table 2. Determinant parameters for photocatalytic performance.

Material	E_g (eV)	Crystal Size (nm)	S_{BET} (m^2 g^{-1})	V_{pore} (m^3 g^{-1})
ZAC	5.66	27.58	18	0.12
ZAC-60S	3.57	31.59	40	0.16
ZAC-80S	3.58	25.47	43	0.16
ZAC-100S	3.67	$11.37_{(003)}$ $37.8_{(111)}$	105	0.30

Figure 6 shows a variation in the width of the hysteresis loop. The literature refers to the width decreasing when the specific area and adsorption capacity decrease too [21], and the results of N_2 physisorption supported it. The sample ZAC-100S showed a larger width and higher adsorption capacity.

The coexistence of two materials origins the formation of heterojunctions that can modify the material's morphology and increase the presence of structural defects such as vacancies. "Those are sites where an atom should be, and it is not there." An increment of "empty sites" results in larger pore volumes. The sample ZAC-100S in N_2 physisorption exhibited the largest pore volume (0.30 m^3 g^{-1}) and agreed with the photoluminescence study, which suggested that this sample has a major percentage of vacancies. In addition, the increment in pore volume can be originated from the ZnS growth between the layers of ZnAl-LDH material.

2.6. Rietveld Analysis and Energy Dispersive Spectrometry (EDS)

Rietveld analysis and EDS for selected samples were carried out to confirm the existence of species such as hydrozincite and cadmium, whose presence has not been confirmed through the characterization techniques used until now. Rietveld analysis was performed for the sample ZAC and ZAC-100S. For Rietveld analysis, the software X'Pert HighScore-Plus was used to identify phases, and Fullprof Suite was used to determine the percentage of each phase. In the supplementary materials section (Figure S1), the sample ZAC showed the crystalline phases of ZnAl-LDH, hydrozincite (HZT), and aluminum hydride (AlH_3) with percentages of 86, 5, and 9%, respectively. Figure 7 shows the Rietveld analysis for the sample ZAC-100S exhibiting the phases ZnS, $CdSO_4$, and ZnAl-LDH at 96.64, 1.71, and 1.65%, respectively. The reliability factors obtained from the Rietveld refinement are the R_{wp}(%) = 10.7, R_{exp}(%) = 8.6, RB(%) = 4.0, and Chi^2 = 1.53.

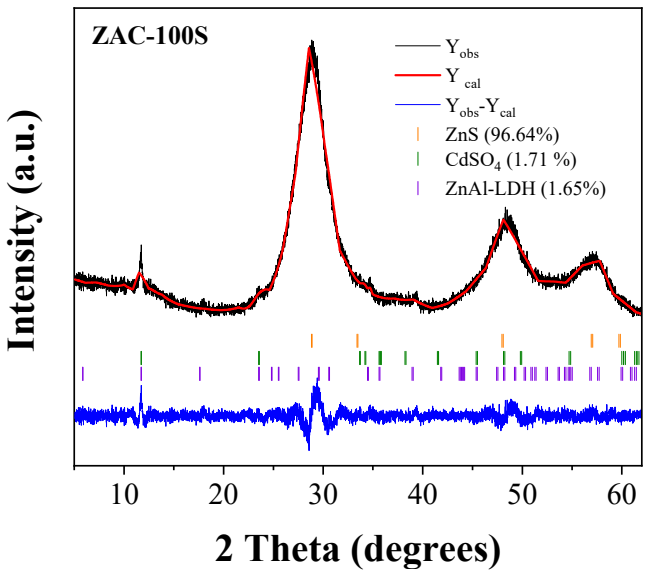

Figure 7. Rietveld analysis for the sample ZAC-100S.

The Rietveld analysis confirmed the presence of hydrozincite in ZAC and cadmium in ZAC-100S. However, the cadmium percentage is extremely low. The EDS technique can explain this (see Figure 8); where it is exhibited, that cadmium is highly dispersed in comparison to Zn, Al, and S. Figure 8 for the sample ZAC-100S shows that Al, Zn, S, and Cd are distributed uniformly in the material, which verifies that a composite material was obtained.

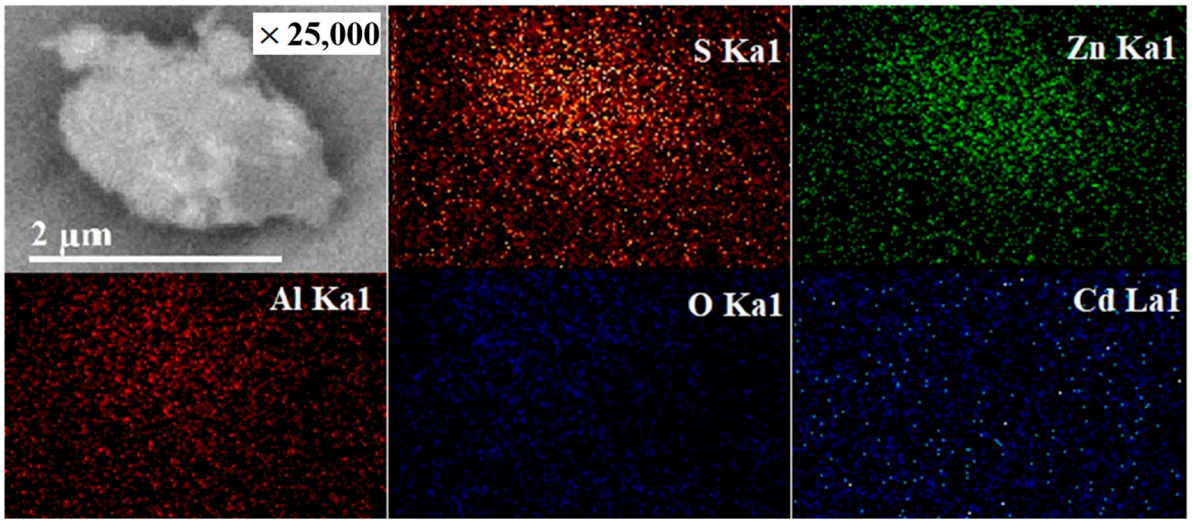

Figure 8. Energy dispersive spectroscopy mapping (EDS), including SEM image for the sample ZAC-100S.

2.7. Scanning Electron Microscopy (SEM) and Transmission Electron Microscopy (TEM)

Figure 9a,b show the morphology of ZAC-100S. Amorphous particles are observed, constituted by the agglomeration of other small spherical particles with a nominal radius of 3.6 µm. The largest particles show a nominal diameter of about 500 nm. Amorphous particles originate from poor crystallization, where the infinitesimal atomic arrangement occurs in limited zones. According to Figure 9c, it is confirmed the ZAC-100S is a composite material with different zones in which the atomic arrangements are too short.

Figure 9c also shows the electron diffraction pattern for the analyzed sample. This result points to the material being polycrystalline. The reflection planes (300), (111), and (20–2) were identified and matched with ZnAl-LDH, ZnS, and $CdSO_4$, respectively. The interplanar distances were measured with Gatan Microscopy Suite Software; Figure 9d–f show the results for each identified zone. The interplanar distance for the plane (20–2) corresponding to $CdSO_4$ was 1.8 Å, for the plane (300) of ZnAl-LDH was 7.5 Å, and the (111) for ZnS was 3.05 Å. The correct identification of the zones and their planes was corroborated by plotting the characteristic crystalline structure of each material through VESTA software (Visualization for Electronic and Structural Analysis) and comparing them with each other.

2.8. Photocatalysis Assessment

Figure 10a shows the photocatalytic assessment; it was carried out under UV light (λ = 270 nm, I = 6.0 mW/m^2) using 20 milligrams of photocatalyst and 250 mL of a methanol-water solution (50-50 vol%). As can be observed, the photocatalysts showed high photoactivity, except for ZAC, which showed almost the same production as photolysis. The efficacy of the materials to produce hydrogen is attributed to the sulfur presence and the sacrificial reagent (methanol); it was observed that the activity is enhanced when the sulfur content is increased. This means that the formation of ZnS and $CdSO_4$ is important in hydrogen production. Figure 10a illustrates that the sample ZAC-100S with the highest sulfur content showed the best hydrogen production, reaching 733 µmol after 5 h of

reaction time and obtaining 10× the amount of hydrogen produced in the methanol-water photolysis, 73 µmol.

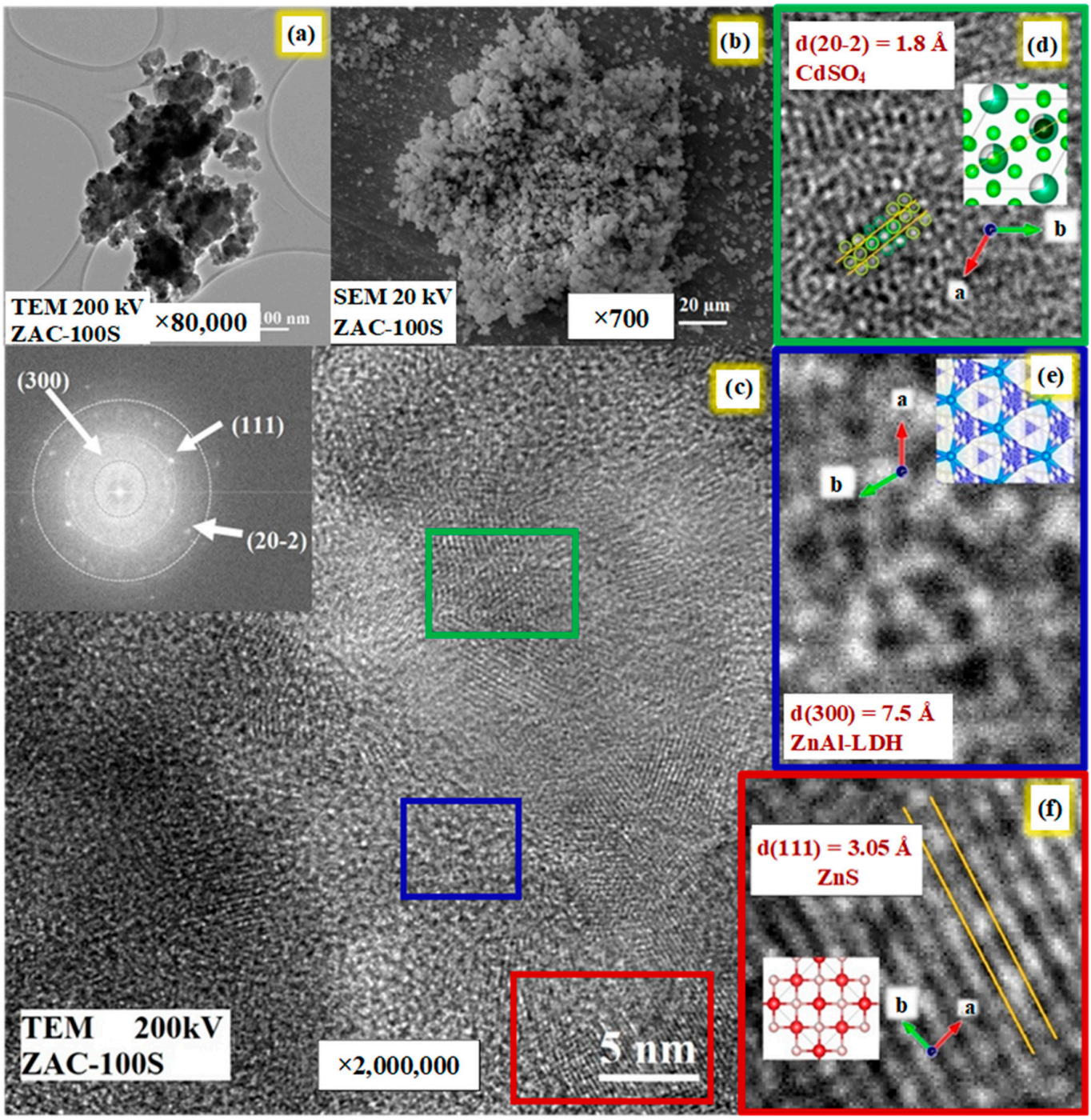

Figure 9. (**a**,**c**–**f**) TEM images on the ZAC-100S sample and interplanar spacing distances, (**b**) SEM image of the ZAC-100S sample.

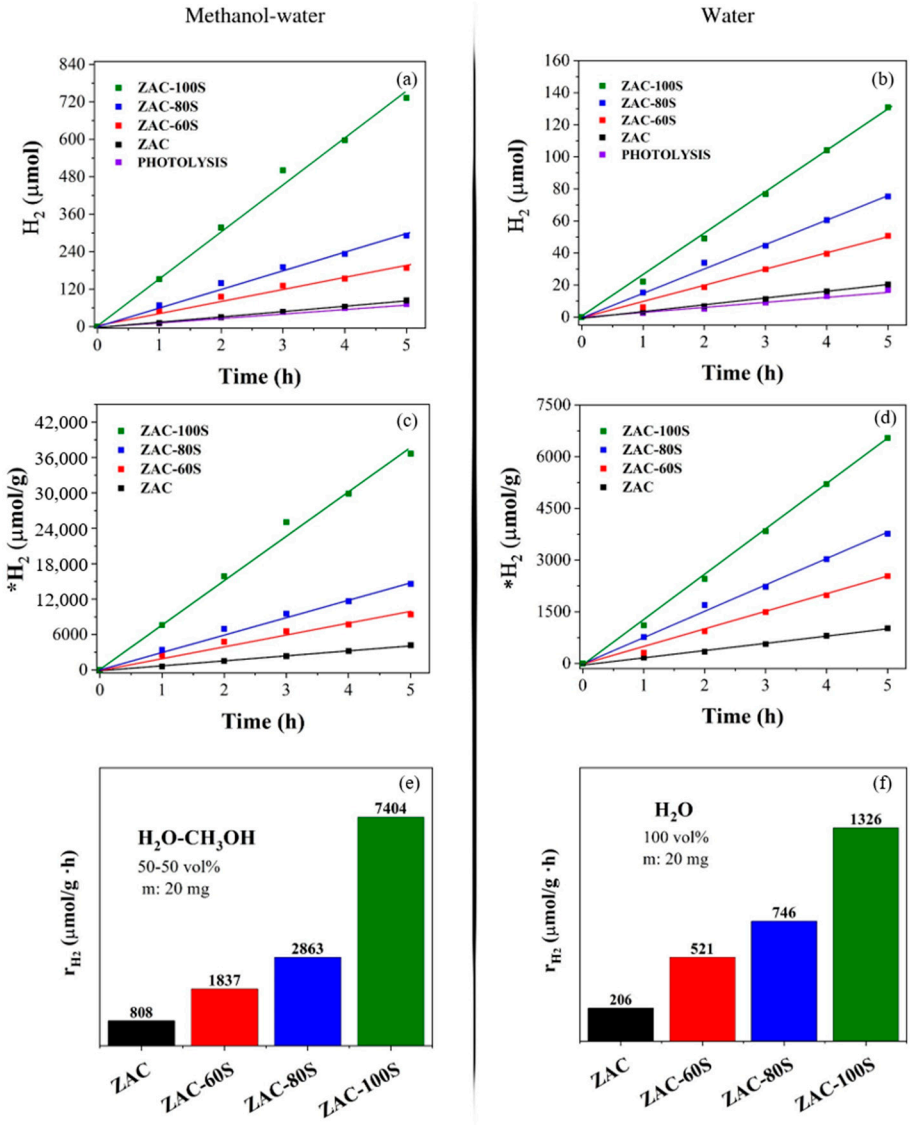

Figure 10. (**a**,**c**,**e**) Results in a methanol-water solution (50-50 vol%); (**b**,**d**,**f**) results without sacrificial reagent; (**a**,**b**) hydrogen production over the time (H_2, µmol); (**c**,**d**) hydrogen produced per gram of photocatalyst (*H_2); and (**e**,**f**) reached rate constants in the hydrogen production (r_{H2}).

Figure 10c shows the hydrogen production per gram of the photocatalyst in the methanol-water solution. These data are important to reactor scale design, where more hydrogen can be obtained when the mass load is greater. Nevertheless, the reactor characteristic should also be modified most of the time. The standardized values indicated that 1 g of the sample ZAC can produce ~4200 µmol at 5 h, whereas the sample ZAC-100S reaches a value of ~37,000 µmol at 5 h. Finally, Figure 10e reveals the standardized rate constants reached for each sample in the hydrogen production; according to this, 1 g of the photocatalyst ZAC produces 808 µmol of hydrogen at 1 h, and 1 g of the photocatalyst ZAC-100S produces 7404 µmol of hydrogen at 1 h.

Figure 10b shows a further photocatalytic assessment; it was carried out under UV light (λ = 270 nm, I = 6.0 mW/m^2) using 20 milligrams of photocatalyst and 250 mL of bidistilled water. As can be observed, the materials can produce hydrogen in the absence of methanol. The amount of hydrogen produced by the sample ZAC-100S was ~131 µmol at 5 h; this is ~8× the amount of hydrogen produced in the water photolysis, 17 µmol at 5 h. Figure 10d,f shows the production per gram of photocatalyst and production per gram of the photocatalyst at 1 h, respectively. Figure 10d shows that 1 g of the photocatalyst ZAC-100S produced ~6600 µmol at 5 h, whereas Figure 10f indicates that 1 g of the sample

had an average value of 1326 µmol at 1 h. The results suggest that the synthesized materials can be an excellent option for producing hydrogen. Furthermore, costs can be reduced since sacrificial reagents such as methanol can be avoided.

2.9. Reaction Mechanism

2.9.1. Charge Carriers' Formation

Figure 11 shows the possible reaction mechanism. The energy of the conduction bands (E_{CB}) and valence bands (E_{VB}) was illustrated according to the values reported in the literature. The materials constituting the composite sample ZAC-100S show the following values of E_g, E_{CB}, and E_{VB}. For ZnAl-LDH ~(3.5 eV, 1.5 eV, −2.0 eV) [22], ZnS ~(3.68 eV, 2.56 eV, −1.12 eV) [23], and $CdSO_4$ ~(3.05 eV, 0.77 eV, 3.82 eV) [24]. A photocatalytic reaction runs when UV light is irradiated over the sample ZAC-100S. First, the material absorbs the photons from UV light; then, they transfer its entire energy to atomic electrons. The incident photon energy (4.6 eV) is higher than the binding energy of certain orbital electrons. Hence, these last will be liberated (e^-) from high-energy orbits, leaving vacancies (h^+) behind. A neighboring electron will occupy the h^+ with lower energy. Thus, the motion of holes through the material is generated, and electrons will be emitted. These electrons have a kinetic energy equal to the incident photon energy minus the binding energy (BE) [25].

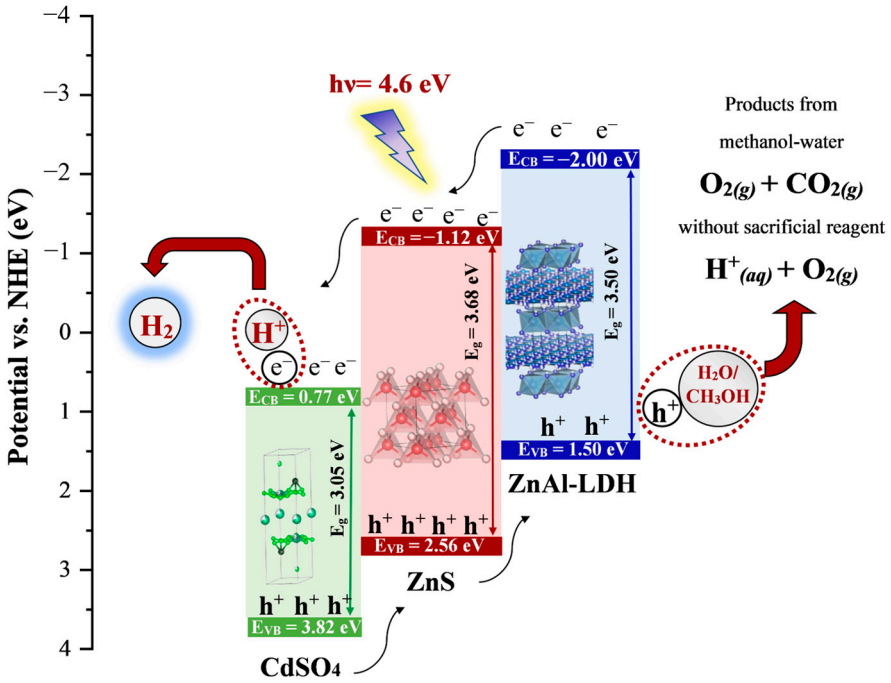

Figure 11. Reaction mechanism on the ZAC-100S sample.

The kinetic energy of the photogenerated electrons (~4.6–BE eV) in Figure 11 is enough to overcome the bandgap energy of the semiconductors $CdSO_4$ (3.05 eV), ZnS (3.68 eV), and ZnAl-LDH (3.50 eV). Therefore, the bandgap in photocatalysis must be understood as the energy required for a photogenerated electron that is bonded in the photocatalyst to become free, and it can participate in oxidation reactions. In this case, the condition is fulfilled.

For the composite system in Figure 11, the photonic absorption is carried out by each compound's most strongly bonded electrons (e.g., K energy shell) because those zones have a high electron concentration. In addition, it is essential to mention that photonic absorption is favored in atoms with a large atomic number [26]. So, it is expected that $CdSO_4$ has more photogenerated electrons and holes. However, it is not entirely true; the presence of heterojunctions type II origins the transference of holes [27]. The vacancies (h^+)

in $CdSO_4$ will be occupied by lower energy electrons present in the valence band of ZnS. Consecutively, the holes in ZnS will be occupied by lower energy electrons in ZnAl-LDH. This does not happen for ZnAl-LDH, since other lower energy electrons do not easily compensate for the electronic deficit. Thus, the presence of the holes in ZnAl-LDH is higher than in $CdSO_4$. The accumulation of electrons in $CdSO_4$ and holes in ZnAl-LDH takes place. Water splitting and photocatalytic reforming have been studied and discussed well. The mechanism for each is summarized below [28,29].

2.9.2. Water Splitting

The reactions performed for the sample ZAC-100S in water are the following. First, holes and electrons photogenerated by UV-light irradiation reach the photocatalyst surface (Equation (2)). Water is adsorbed on the photocatalyst surface and reacts with the photogenerated holes (h^+) to produce oxygen and hydrogen protons (H^+) (Equation (3)). The hydrogen protons react with the photogenerated electrons to produce hydrogen (Equation (4)). It is also possible that the photogenerated electrons carry out the direct reduction of water (Equation (5)). For the present case, the synthesis of a composite material allowed an adequate charge carriers separation; the recombination between holes and electrons was minimized, so many of them reached the surface to achieve a rate constant of hydrogen production of 1326 μmol/g·h.

Hole and electron formation:

$$ZAC - 100S \xrightarrow{h\nu} h^+ + e^- \quad (2)$$

Oxidation:

$$2H_2O_{(l)} + 4h^+ \rightarrow 4H^+_{(aq)} + O_{2\ (g)} \quad (3)$$

Successive reaction of reduction:

$$4H^+_{(aq)} + 4e^- \rightarrow 2H_{2\ (g)} \quad (4)$$

Direct reaction of reduction:

$$2H_2O_{(l)} + 2e^- \rightarrow H_{2\ (g)} + OH^-_{(aq)} \quad (5)$$

2.9.3. Photocatalytic Reforming

The current study is partially a photocatalytic reforming because it used a methanol-water solution (50-50 vol%). Here, the aim is for methanol, CH_3OH, to act as a sacrificial reagent. The reaction mechanism in a methanol-water solution for experiments in Figure 10a,b using the samples ZAC-XS% will now be described. Reactions (Equations (2)–(5)) are carried out like water splitting. However, the inverse reaction for oxidation can take place in water splitting (Equation (6)). This is not desirable because the number of available electrons would be diminished to carry out the subsequent reaction (Equation (4)). Equations (4) and (6) are competing reactions and can lead to the $H^+_{(aq)}$ depletion that is reflected as a hydrogen production decrement. Adding CH_3OH to the reaction media minimizes the e^-/h^+ recombination. The holes, h^+, participate in an oxidation process to photodegrade the alcohol, allowing the "free performance" of the electrons in water reduction. The photodegradation of CH_3OH is an oxidative process and consumes oxygen; the necessary process to perform Equation (6) takes place. Therefore, the probability of an inverse reaction will be minor, and hydrogen production will be improved.

Inverse reaction:

$$4H^+_{(aq)} + O_{2\ (g)} + 4e^- \rightarrow 2H_2O_{(l)} \quad (6)$$

3. Materials and Methods

3.1. Synthesis of the LDH Materials

The synthesis of the hydrotalcite ZnAlCd compound was obtained by the chemical coprecipitation of the salts $Zn(NO_3)_2$, $Al(NO_3)_3$, and $Cd(NO_3)_2$. In a one-liter, flat-bottomed flask with 800 mL of bidistilled water, the precursor salts were added in a mol ratio Zn: Al, 3:1, keeping the mol percentages of ZnAl:Cd at 94:6. Urea was added to promote the hydrolyzation reaction and an alkaline media of pH 8.5. Once the salts and urea were dissolved, the solution in the flask was kept at 98 °C and 350 rpm (stirring rate). Under previous conditions, the flask was connected to a condenser to avoid water evaporation and kept thus for 72 h. After this time, the precipitated material was filtered and washed several times with bidistilled water at 80 °C. Subsequently, the filtered material was dried in a muffle furnace at 80 °C for 12 h. Finally, the support material was crushed in a mortar and labeled as ZAC.

3.2. ZAC Sulfuration

The variation of the sulfur amount was realized with respect to the nominal amount of the Zn^{2+} cation; the added percentages of sulfur were 60, 80, and 100 mol% to Zn^{2+}, respectively. In a Parr reactor with 100 mL of ethanol and 0.5 mL of ethylenediamine, 1 g of LDH support ZAC was added. Then, thiourea was added in the appropriate amounts. Next, the reactor Parr was kept under 40 psi and 135 °C for 5 h. Once the aging period was finished, the material was filtered and washed with bidistilled water at 80 °C. Finally, the material was dried at 80 °C for 24 h, crushed in a mortar, and labeled as ZAC-60S, ZAC-80S, and ZAC-100S.

3.3. Characterization of the Powder Photocatalysts

Diffuse Reflectance Spectroscopy UV-Vis (DRS). This was carried out in a Varian Cary 100 spectrometer (Mulgrave, Vic, Australia) equipped with an integrating sphere, and $BaSO_4$ was used as a reference sample. Fourier Transform Infrared Spectroscopy (FTIR). The absorption spectra were recorded in an Affinity-1 Shimadzu IR-440 (Kyoto, Tapan) from 500 to 4000 cm^{-1} with a resolution of 8.0 cm^{-1} and 250 scans. X-ray Diffraction (XRD). A Bruker D2 (Billerica, MA, USA) was used with a radiation source of Cu Kα (50 kV 40 mA). The diffractograms were obtained at 0.3°/s from 5 to 70° of 2θ, and a step size of 0.01°. Photoluminescence (PL). The photoluminescence spectra were realized in a SCINCO FS-2 Fluorescence Spectrometer (Seoul, Republic of Korea) with a wavelength of excitation equal to 299 nm, a slit of 10 nm, and a scan speed of 300 nm/min. Physisorption of N_2. Isotherms were obtained using Quantachrome Autosorb-3B equipment (Boynton Beach, FL, USA); before the analysis, the samples were degassed at 80 °C for 24 h, and the BET method determined the surface area. Microscopies (SEM and TEM). The modification of the morphology of the samples was studied with a JEOL JSM-7600f Scanning Electron Microscope (Tokyo, Japan) operating at 20 kV and equipped with energy-dispersive X-ray spectroscopy (Oxford X-Max). The atomic arrangement, several constituting compounds' presence, and heterojunction formation were analyzed through Transmission Electron Microscopy with a JEM2100 microscope (Tokyo, Japan) with LaB6 filament and 200 kV acceleration voltage.

3.4. Photocatalysts Assessment

The reaction for hydrogen production was carried out in a glass batch reactor. For photocatalytic assessment, a heterogeneous solution was prepared with 200 mL of a methanol-water solution (50-50 vol%) and a photocatalyst load of 20 mg. The reaction was performed under UV light using a UV Pen-ray lamp (λ = 270 nm, I = 6.0 mW/m^2). The lamp was covered with a quartz tube that then was submerged in the heterogeneous solution and centered. The reaction lasted 5 h with a stirring rate of 800 rpm. A Shimadzu G6-8A gas chromatographer determined the hydrogen production with a thermal conductivity detector (TDC) and a Shin-carbon column; N_2 was used as a carrier gas.

4. Conclusions

The composite samples ZAC-XS were successfully synthesized and assessed for hydrogen production. The materials were corroborated as heterogeneous nature where the addition of sulfur modified the crystal growth of each constituting component and caused a significant increment in the specific surface area, which resulted in improved absorption and high photoactivity. The band gap energy was also reduced, making it adequate for photon absorption. The simultaneous presence of $CdSO_4$, ZnS, and ZnAl-LDH favored the formation of heterojunctions, making the hole and electron transfer easier and allowing the correct charge carrier separation. An ideal charge separation was demonstrated in water splitting, even though hydrogen production is increased when methanol is used as a sacrificial reagent. The results obtained in this paper encourages further research into uncalcined samples and to look for an adequate composite system whose valence and conduction bands allow hydrogen production without a sacrificial reagent.

Supplementary Materials: The following supporting information can be downloaded at: https://www.mdpi.com/article/10.3390/catal13030593/s1, Figure S1: Rietveld Analysis for the sample ZAC.

Author Contributions: A.G.R.-V.: conceptualization, methodology, validation, formal analysis, investigation, data curation, writing-original draft. C.T.-F.: data curation, writing original draft, visualization. R.P.H.: visualization, resources, supervision, project administration. A.B.-R.: visualization, resources, supervision, project administration. F.T.: conceptualization, supervision, project administration, funding acquisition. R.G.: resources, supervision, project administration, funding acquisition. All authors have read and agreed to the published version of the manuscript.

Funding: This research was funded by the Consejo Nacional de Ciencia y Tecnología (CONACyT) with financial support to the students with CVU 507714, CVU 739220, and the research project number A1-S-41124.

Data Availability Statement: The data presented in this study are available on request from the corresponding author.

Acknowledgments: Angela. G. Romero-Villegas thanks every member of the Ecocatalysis department from Universidad Autónoma Metropolitana-Iztapalapa, the co-authors for their essential collaboration, and the reviewers for supporting this research.

Conflicts of Interest: The authors declare no conflict of interest.

References

1. Farias, C.B.B.; Barreiros, R.C.S.; da Silva, M.F.; Casazza, A.A.; Converti, A.; Sarubbo, L.A. Use of Hydrogen as Fuel: A Trend of the 21st Century. *Energies* **2022**, *15*, 311. [CrossRef]
2. Kundu, B.K.; Han, G.; Sun, Y. Derivatized Benzothiazoles as Two-Photon-Absorbing Organic Photosensitizers Active under Near Infrared Light Irradiation. *J. Am. Chem. Soc.* **2023**, *145*, 3535–3542. [CrossRef]
3. Tzompantzi-Flores, C.; Castillo-Rodríguez, J.C.; Gómez, R.; Hernández, R.P.; Santolalla-Vargas, C.E.; Tzompantzi, F. Photocatalytic Evaluation of the ZrO_2:$Zn_5(OH)_6(CO_3)_2$ Composite for the H_2 Production via Water Splitting. *Top. Catal.* **2020**, *63*, 575–585. [CrossRef]
4. Chubar, N.; Gilmour, R.; Gerda, V.; Mičušík, M.; Omastova, M.; Heister, K.; Man, P.; Fraissard, J.; Zaitsev, V. Layered double hydroxides as the next generation inorganic anion exchangers: Synthetic methods versus applicability. *Adv. Colloid Interface Sci.* **2017**, *245*, 62–80. [CrossRef]
5. Kaur, H.; Singh, S.; Pal, B. A brief review on modified layered double hydroxides for H_2 production through photoinduced H_2O splitting. *Environ. Nanotechnol. Monit. Manag.* **2021**, *16*, 100451. [CrossRef]
6. Li, A.; Deng, H.; Ye, C.; Jiang, Y. Fabrication and characterization of novel ZnAl-layered double hydroxide for the superadsorption of organic contaminants from wastewater. *ACS Omega* **2020**, *5*, 15152–15161. [CrossRef]
7. Suárez-Quezada, M.; Romero-Ortiz, G.; Samaniego-Benítez, J.; Suárez, V.; Mantilla, A. H_2 production by the water splitting reaction using photocatalysts derived from calcined ZnAl LDH. *Fuel* **2018**, *240*, 262–269. [CrossRef]
8. He, X.; Qiu, X.; Chen, J. Preparation of Fe(II)–Al layered double hydroxides: Application to the adsorption/reduction of chromium. *Colloids Surf. A Physicochem. Eng. Asp.* **2016**, *516*, 362–374. [CrossRef]
9. Rodriguez-Rivas, F.; Pastor, A.; de Miguel, G.; Cruz-Yusta, M.; Pavlovic, I.; Sánchez, L. Cr^{3+} substituted Zn-Al layered double hydroxides as UV–Vis light photocatalysts for NO gas removal from the urban environment. *Sci. Total Environ.* **2019**, *706*, 136009. [CrossRef]

10. Zhang, J.; Shen, B.; Hu, Z.; Zhen, M.; Guo, S.-Q.; Dong, F. Uncovering the synergy between Mn substitution and O vacancy in ZnAl-LDH photocatalyst for efficient toluene removal. *Appl. Catal. B Environ.* **2021**, *296*, 120376. [CrossRef]
11. Nguyen, T.K.N.; Matsui, Y.; Shirahata, N.; Dumait, N.; Cordier, S.; Grasset, F.; Ohashi, N.; Uchikoshi, T. Zn-Al layered double hydroxide-based nanocomposite functionalized with an octahedral molybdenum cluster exhibiting prominent photoactive and oxidation properties. *Appl. Clay Sci.* **2020**, *196*, 105765. [CrossRef]
12. Gil, J.J.; Aguilar-Martínez, O.; Piña-Pérez, Y.; Pérez-Hernández, R.; Santolalla-Vargas, C.; Gómez, R.; Tzompantzi, F. Efficient ZnS–ZnO/ZnAl-LDH composite for H_2 production by photocatalysis. *Renew. Energy* **2019**, *145*, 124–132. [CrossRef]
13. Thite, V.D.; Giripunje, S.M. Adsorption and photocatalytic performance of ZnAl layered double hydroxide nanoparticles in removal of methyl orange dye. *Nanotechnol. Environ. Eng.* **2022**, *7*, 57–66. [CrossRef]
14. Mendoza-Damián, G.; Tzompantzi, F.; Mantilla, A.; Pérez-Hernández, R.; Hernández-Gordillo, A. Improved photocatalytic activity of SnO_2–ZnAl LDH prepared by one step Sn^{4+} incorporation. *Appl. Clay Sci.* **2016**, *121–122*, 127–136. [CrossRef]
15. Lalithadevi, B.; Rao, K.M.; Ramananda, D. Investigations on structural and optical properties of starch capped ZnS nanoparticles synthesized by microwave irradiation method. *Chem. Phys. Lett.* **2018**, *700*, 74–79. [CrossRef]
16. Tzompantzi, F.; Tzompantzi-Flores, C.; Portillo-Vélez, N.; Castillo-Rodríguez, J.; Gómez, R.; Hernández, R.P.; Santolalla-Vargas, C. Preparation and characterization of the polycrystalline material $Zn_5(OH)_6(CO_3)_2$. Determination of the active species in oxide-reduction processes. *Fuel* **2020**, *281*, 118471. [CrossRef]
17. Torres-Ricárdez, R.; Lizama-Tzec, F.; García-Mendoza, M.; Ramírez-Morales, E.; Rojas-Blanco, L.; Ramírez-Betancour, R.; Martínez-Solís, F.; Pérez-Hernández, G. Electrodeposited stoichiometric zinc sulfide films. *Ceram. Int.* **2020**, *46*, 10490–10494. [CrossRef]
18. Kundu, B.K.; Das, M.; Ganguly, R.; Bhobe, P.A.; Mukhopadhyay, S. Role of zeolite encapsulated Cu(II) complexes in electron transfer as well as peroxy radical intermediates formation during oxidation of thioanisole. *J. Catal.* **2020**, *389*, 305–316. [CrossRef]
19. Kundu, B.K.; Chhabra, V.; Malviya, N.; Ganguly, R.; Mishra, G.S.; Mukhopadhyay, S. Zeolite encapsulated host-guest Cu(II) Schiff base complexes: Superior activity towards oxidation reactions over homogenous catalytic systems. *Microporous Mesoporous Mater.* **2018**, *271*, 100–117. [CrossRef]
20. Berlin, I.J.; Anitha, V.S.; Thomas, P.V.; Joy, K. Influence of oxygen atmosphere on the photoluminescence properties of sol–gel derived ZrO_2 thin films. *J. Sol-Gel Sci. Technol.* **2012**, *64*, 289–296. [CrossRef]
21. Saiah, F.B.D.; Su, B.-L.; Bettahar, N. Nickel–iron layered double hydroxide (LDH): Textural properties upon hydrothermal treatments and application on dye sorption. *J. Hazard. Mater.* **2009**, *165*, 206–217. [CrossRef]
22. Bian, X.; Zhang, S.; Zhao, Y.; Shi, R.; Zhang, T. Layered double hydroxide-based photocatalytic materials toward renewable solar fuels production. *Infomat* **2021**, *3*, 719–738. [CrossRef]
23. Wu, A.; Jing, L.; Wang, J.; Qu, Y.; Xie, Y.; Jiang, B.; Tian, C.; Fu, H. ZnO-dotted porous ZnS cluster microspheres for high efficient, Pt-free photocatalytic hydrogen evolution. *Sci. Rep.* **2015**, *5*, srep08858. [CrossRef]
24. Materials Data on $CdSO_4$, Materials Project, United States. 2020. Available online: https://materialsproject.org/materials/mp-5679 (accessed on 20 December 2022).
25. Spagnolo, G.S.; Postiglione, A.; De Angelis, I. Simple equipment for teaching internal photoelectric effect. *Phys. Educ.* **2020**, *55*, 055011. [CrossRef]
26. Hussein, E.M.A. (Ed.) Chapter one-mechanisms. In *Radiation Mechanics*; Elsevier Science Ltd.: Oxford, UK, 2007; pp. 1–65. [CrossRef]
27. Tan, X.; Ng, S.; Mohamed, A.R.; Ong, W. Point-to-face contact heterojunctions: Interfacial design of 0D nanomaterials on 2D g-C_3N_4 towards photocatalytic energy applications. *Carbon Energy* **2022**, *4*, 665–730. [CrossRef]
28. Takata, T.; Jiang, J.; Sakata, Y.; Nakabayashi, M.; Shibata, N.; Nandal, V.; Seki, K.; Hisatomi, T.; Domen, K. Photocatalytic water splitting with a quantum efficiency of almost unity. *Nature* **2020**, *581*, 411–414. [CrossRef]
29. Guzman, F.; Chuang, S.S.C.; Yang, C. Role of Methanol Sacrificing Reagent in the Photocatalytic Evolution of Hydrogen. *Ind. Eng. Chem. Res.* **2013**, *52*, 61–65. [CrossRef]